Faraday instability in double-interface fluid layers

Kevin Ward*
Department of Chemical Engineering, University of Florida, 1030 Center Drive, Gainesville, Florida 32611, USA
and IEMN, University of Lille, CNRS, UMR No. 8520, 59000 Lille, France

Farzam Zoueshtiagh
IEMN, University of Lille, CNRS, UMR No. 8520, 59000 Lille, France

Ranga Narayanan†
Department of Chemical Engineering, University of Florida, 1030 Center Drive, Gainesville, Florida 32611, USA

(Received 25 May 2018; published 10 April 2019)

We investigate, both by way of theory and by experiments, the mechanically forced Faraday instability in immiscible three-fluid systems that is two-interface fluid layers. The theoretical model suggests that two-interface fluid layers offer underlying physics quite distinct from the typical single-interface system due to the coupling of the fluid interfaces, resulting in alternating double-tongued stability curves. This allows for the possibility of unique codimension points unattainable in traditional two-fluid systems. In addition, the presence of a third fluid in the problem can lead to either enhanced or delayed destabilization of the system at target frequencies. Experimental results qualitatively support the theory, though precise agreement between the theory and the experiment is hindered due to the sidewall damping.

DOI: 10.1103/PhysRevFluids.4.043903

I. INTRODUCTION

Since its initial discovery [1], Faraday instability has been studied extensively both by way of theory and by way of experiments. The driving mechanism for the instability is the resonance between an imposed oscillation frequency and a system's natural frequency, leading to the generation of interfacial patterns when a critical forcing acceleration is reached. These patterns typically appear subharmonic to the forcing frequency [2] and can occur with a large range of wavelengths depending on the system parameters [3–6].

Theoretical prediction of the stability thresholds began with Benjamin and Ursell [7], who studied the linear stability of an inviscid system. Later research by Kumar and Tuckerman [8] served to incorporate viscosity into the model to combat discrepancies between theory and experiment observed by other researchers [9–11]. This model was derived from a rigorous linear stability analysis conducted on a two-fluid laterally unbounded mechanically oscillated system. Bechhoefer *et al.* [12] performed experiments and utilized the model to accurately predict minimum stability thresholds, while Batson *et al.* [13] verified it further utilizing a small cylindrical geometry with fluids that respected the assumptions of the model.

*klward3@ufl.edu
†ranga@ufl.edu

To date, most research in the field has been conducted on two-fluid systems. However, ultimate applications of the instability, including mixing enhancement [14], atomization [15], or intentional suppression of the instability, could benefit from additional control over the instability thresholds and modal structures. Previous research has highlighted additional physics through many extensions of the traditional problem, including the use of flexible boundaries [16], multiple forcing frequencies and unique forcing functions [17–19], or pre-patterned surfaces [20]. Bestehorn and Pototsky [21] utilized a reduced-order nonlinear model to study the instability, with a third passive fluid present above two thin liquid films, and observed the occurrence of a double-minimum tongue. Introducing an additional fluid, and consequently an additional interface, to the problem could allow end users to tailor the instability characteristics within a given system in a beneficial manner. This possibility forms the motivation for the present work, in which the effects of adding a third fluid to the physics of the instability are examined both experimentally and theoretically.

The examined system mechanically oscillates with a single forcing frequency and all three fluids are immiscible, viscous, and contained within cylindrical geometries for experiments. Through the addition of a third fluid, the instability thresholds for a given system can be modified in both stabilizing and destabilizing manners. Of additional interest is the modal response within these three-fluid systems, where coupling between the interfaces can allow for unique codimension points unobtainable with two-fluid systems under the same forcing conditions. These responses could be of particular interest to applications where a unique interfacial shape is sought, such as the creation of a metamaterial [22,23].

In the present work, we first present the theoretical model, which extends Kumar and Tuckerman's [8] theory to introduce the possibility of coupling effects between multiple interfaces. After derivation of the model, a theoretical comparison of the results to those found for similar two-fluid Faraday instability systems is given. The distinct physics arising due to the third fluid is explained and test cases showing both stabilizing and destabilizing effects are presented. Next, experimentally measured stability thresholds are compared to the theoretical predictions for two separate cylindrical geometries. The fluids chosen for the experiments are those used by Batson *et al.* [13] in addition to water, as these were found to best satisfy all the necessary experimental requirements, including safety, immiscibility, and suitable density differences. The favorable qualitative agreement lends credibility to the present theoretical model.

II. THEORETICAL MODEL

The theoretical model follows closely that first derived by Kumar and Tuckerman [8]. As in their model, we opt to use unscaled variables and equations in order to make a comparison with experiments and also because there is no particular advantage in introducing a large number of dimensionless groups, such as property ratios, for a multilayer system. A linear stability analysis is performed on an initially quiescent, horizontally infinite three-fluid system as shown in Fig. 1.

The hydrodynamics in all three fluids are governed by the Navier-Stokes equations adapted to a moving reference frame coupled with the continuity equations, given in unscaled form by

$$\rho_j\left(\frac{\partial \boldsymbol{V}_j}{\partial t} + \boldsymbol{V}_j \cdot \boldsymbol{\nabla}\boldsymbol{V}_j\right) = -\boldsymbol{\nabla}P_j + \mu_j \nabla^2 \boldsymbol{V}_j - \rho_j[g + A\omega^2 \cos(\omega t)]\boldsymbol{i}_z \tag{1}$$

and

$$\boldsymbol{\nabla} \cdot \boldsymbol{V}_j = 0, \tag{2}$$

where $\boldsymbol{V}$ is the fluid velocity, P is the pressure, μ is the viscosity, ρ is the density, g is gravitational acceleration, A is the forcing amplitude, ω is the forcing frequency, and $j = 1, 2, 3$ denotes the bottom, middle, and top fluids, respectively. This description is completed by the boundary conditions.

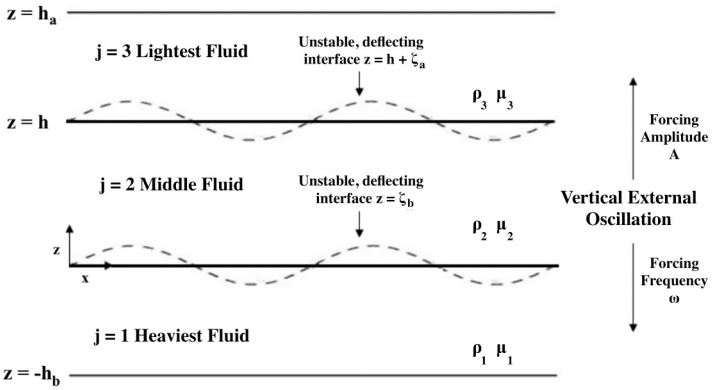

FIG. 1. Schematic of the three-fluid mechanically oscillated system. The normal vectors point into the lighter fluid at each interface. The lower interface is taken to be located at $z = 0$ and both interfaces are initially flat.

At the upper and lower walls we have no slip and no penetration and at the top interface $z = h + \zeta_a(x, t)$ we have

$$[[\boldsymbol{V}_j \cdot \boldsymbol{n_a}]]_a = 0, \tag{3}$$

$$[[\boldsymbol{V}_j \cdot \boldsymbol{t_a}]]_a = 0, \tag{4}$$

$$[[\boldsymbol{n_a} \cdot \underline{\underline{T_j}} \cdot \boldsymbol{n_a}]]_a = \gamma_a 2H_a, \tag{5}$$

$$[[\boldsymbol{n_a} \cdot \underline{\underline{T_j}} \cdot \boldsymbol{t_a}]]_a = 0. \tag{6}$$

At the bottom interface $z = \zeta_b(x, t)$ we have

$$[[\boldsymbol{V}_j \cdot \boldsymbol{n_b}]]_b = 0, \tag{7}$$

$$[[\boldsymbol{V}_j \cdot \boldsymbol{t_b}]]_b = 0, \tag{8}$$

$$[[\boldsymbol{n_b} \cdot \underline{\underline{T_j}} \cdot \boldsymbol{n_b}]]_b = \gamma_b 2H_b, \tag{9}$$

$$[[\boldsymbol{n_b} \cdot \underline{\underline{T_j}} \cdot \boldsymbol{t_b}]]_b = 0. \tag{10}$$

The immiscibility of the fluids requires that at each interface we have

$$[[\rho_j(\boldsymbol{V}_j - \boldsymbol{U}_a) \cdot \boldsymbol{n}_a]]_a = 0 \tag{11}$$

and

$$[[\rho_j(\boldsymbol{V}_j - \boldsymbol{U}_b) \cdot \boldsymbol{n}_b]]_b = 0, \tag{12}$$

where $[[\theta_j]]_a$ denotes $\theta_3 - \theta_2$, $[[\theta_j]]_b$ denotes $\theta_2 - \theta_1$, $\boldsymbol{n}$ is the unit normal vector pointing into the lighter fluid, $\boldsymbol{t}$ is the unit tangent vector, $\boldsymbol{U} \cdot \boldsymbol{n}$ is the interfacial speed, γ_a and $2H_a$ are the interfacial tension and twice the mean surface curvature of the top interface, respectively, and γ_b and $2H_b$ are the interfacial tension and twice the mean surface curvature at the bottom interface, respectively.

The equations are linearized about a quiescent nondeflecting base state by expanding the dependent variables as $\boldsymbol{V} = \boldsymbol{V}'$ and $P = P_0 + P'$. Similar expansions are used for the interface variables ζ, $\boldsymbol{n}$, $\boldsymbol{t}$, and $2H$. In the above, the subscript 0 denotes the base state and the prime denotes

the perturbed state. Applying these expansions yields the base state domain equations

$$\frac{\partial P_{0j}}{\partial z} = -\rho_j(g + A\omega^2 \cos \omega t) \tag{13}$$

and the perturbed domain equations

$$\rho_j \frac{\partial \boldsymbol{V}'_j}{\partial t} = -\nabla P'_j + \mu_j \nabla^2 \boldsymbol{V}'_j. \tag{14}$$

The pressure is eliminated by first applying the double curl to (14) and then using the continuity equation, resulting in

$$\rho_j \partial t \nabla^2 \boldsymbol{V}'_j = \mu_j \nabla^4 \boldsymbol{V}'_j. \tag{15}$$

As in Ref. [8], a Floquet expansion is used in order to separate variables, viz.,

$$\psi(x, z, t) = e^{ikx} \sum_{n=-\infty}^{\infty} e^{[\sigma + i(\alpha + n\omega)]t} \hat{\psi}_n(z), \tag{16}$$

where α can take the value of 0 or $\frac{\omega}{2}$ to allow for harmonic and subharmonic responses and σ is the growth rate. This results in the final perturbed domain equation

$$\left[\sigma + i(\alpha + n\omega) - \nu_j\left(\frac{d^2}{dz^2} - k^2\right)\right]\left(\frac{d^2}{dz^2} - k^2\right)W_{nj} = 0 \tag{17}$$

and its accompanying boundary conditions (dropping the circumflexes)

$$W_{n1} = 0, \tag{18}$$

$$\frac{dW_{n1}}{dz} = 0 \tag{19}$$

at $z = -h_b$;

$$W_{n3} = 0, \tag{20}$$

$$\frac{dW_{n3}}{dz} = 0 \tag{21}$$

at $z = h_a$;

$$W_{n1} = W_{n2}, \tag{22}$$

$$\frac{dW_{n1}}{dz} = \frac{dW_{n2}}{dz}, \tag{23}$$

$$\mu_1\left(\frac{d^2}{dz^2} + k^2\right)W_{n1} = \mu_2\left(\frac{d^2}{dz^2} + k^2\right)W_{n2}, \tag{24}$$

$$[\sigma + i(\alpha + n\omega)]\zeta'_b = W_{n2} = W_{n1} \tag{25}$$

at $z = 0$; and

$$W_{n3} = W_{n2}, \tag{26}$$

$$\frac{dW_{n3}}{dz} = \frac{dW_{n2}}{dz}, \tag{27}$$

$$\mu_3\left(\frac{d^2}{dz^2}+k^2\right)W_{n3}=\mu_2\left(\frac{d^2}{dz^2}+k^2\right)W_{n2}, \tag{28}$$

$$[\sigma+i(\alpha+n\omega)]\zeta_a'=W_{n2}=W_{n3} \tag{29}$$

at $z=h$, where W_n is the z component of the perturbed velocity. Equation (17) is an ordinary differential equation, whose solutions take the form

$$W_{nj}=A_{nj}e^{kz}+B_{nj}e^{-kz}+C_{nj}e^{q_nz}+D_{nj}e^{-q_nz}, \tag{30}$$

where $q_n=\sqrt{\frac{\sigma+i(\alpha+n\omega)}{\nu_j}+k^2}$. It should be noted that when $q_n=k$, the solution instead takes the form

$$W_{nj}=A_{nj}e^{kz}+B_{nj}e^{-kz}+C_{nj}ze^{kz}+D_{nj}ze^{-kz}. \tag{31}$$

At this point, the unknown coefficients are calculated by casting the system of equations into a 12×12 matrix and solving via inversion. This results in expressions for the velocity profiles in all three fluids in terms of ζ_a' and ζ_b'. The coupling between the two interfaces results from the presence of the middle fluid in Eqs. (25) and (29). The next step is to simplify the normal components of the stress balances at both interfaces, which ultimately govern the stability of the entire system:

$$\left[\left[-\left(P_j'+\zeta_a'\frac{dP_0}{dz}\right)+2\mu_j\frac{dW_j}{dz}\right]\right]_a=\gamma_a\nabla_H^2\zeta_a' \quad \text{at } z=h \tag{32}$$

and

$$\left[\left[-\left(P_j'+\zeta_b'\frac{dP_0}{dz}\right)+2\mu_j\frac{dW_j}{dz}\right]\right]_b=\gamma_b\nabla_H^2\zeta_b' \quad \text{at } z=0. \tag{33}$$

Taking ∇_H^2 of these equations and substituting the base state pressure term given by Eq. (13) yields

$$\left[\left[-\nabla_H^2P_j'+\nabla_H^2[\rho_j(g+A\omega^2\cos\omega t)]\zeta_a'+2\mu_j\nabla_H^2\frac{dW_j}{dz}\right]\right]_a=\gamma_a\nabla_H^4\zeta_a' \quad \text{at } z=h \tag{34}$$

and

$$\left[\left[-\nabla_H^2P_j'+\nabla_H^2[\rho_j(g+A\omega^2\cos\omega t)]\zeta_b'+2\mu_j\nabla_H^2\frac{dW_j}{dz}\right]\right]_b=\gamma_b\nabla_H^4\zeta_b' \quad \text{at } z=0. \tag{35}$$

Taking ∇_H of Eq. (14) and then utilizing the continuity equation yields an expression for $\nabla_H^2P_j'$,

$$\nabla_H^2P_j'=\left(\rho_j\frac{\partial}{\partial t}-\mu_j\nabla^2\right)\frac{\partial W_j}{\partial z}, \tag{36}$$

which upon substitution into Eqs. (34) and (35) and expanding variables using (16) yields

$$\left[\left[\rho_j[\sigma+i(\alpha+n\omega)]\frac{\partial W_{nj}}{\partial z}-\mu_j\frac{d^3W_{nj}}{dz^3}+k^2\left\{\rho_j\left(g\zeta_{a,n}'+\frac{A\omega^2}{2}(\zeta_{a,n-1}'+\zeta_{a,n+1}')\right)\right\}+3\mu_jk^2\frac{dW_{nj}}{dz}\right]\right]_a=\gamma_ak^4\zeta_{a,n}' \tag{37}$$

and

$$\left[\left[\rho_j[\sigma+i(\alpha+n\omega)]\frac{\partial W_{nj}}{\partial z}-\mu_j\frac{d^3W_{nj}}{dz^3}+k^2\left\{\rho_j\left(g\zeta_{b,n}'+\frac{A\omega^2}{2}(\zeta_{b,n-1}'+\zeta_{b,n+1}')\right)\right\}+3\mu_jk^2\frac{dW_{nj}}{dz}\right]\right]_b=\gamma_bk^4\zeta_{b,n}' \tag{38}$$

at $z = h$ and $z = 0$, respectively. Upon rearranging we obtain

$$\left[\left[\rho_j[\sigma + i(\alpha + n\omega) + 3\mu_j k^2]\frac{dW_{nj}}{dz} - \mu_j\frac{d^3W_{nj}}{dz^3}\right]\right]_a + [(\rho_3 - \rho_2)g - \gamma k^2]k^2\zeta'_{a,n}$$
$$= -\frac{A\omega^2(\rho_3 - \rho_2)k^2}{2}(\zeta'_{a,n-1} + \zeta'_{a,n+1}) \tag{39}$$

and

$$\left[\left[\rho_j[\sigma + i(\alpha + n\omega) + 3\mu_j k^2]\frac{dW_{nj}}{dz} - \mu_j\frac{d^3W_{nj}}{dz^3}\right]\right]_b + [(\rho_2 - \rho_1)g - \gamma k^2]k^2\zeta'_{b,n}$$
$$= -\frac{A\omega^2(\rho_2 - \rho_1)k^2}{2}(\zeta'_{b,n-1} + \zeta'_{b,n+1}), \tag{40}$$

where the expressions for W_{nj} are given by the evaluation of the solutions to Eq. (30) after application of the boundary conditions at the appropriate z location. Upon inspection, it can be seen that these expressions contain both $\zeta'_{a,n}$ and $\zeta'_{b,n}$ terms for all values of j due to the coupling of the velocity profiles through the middle fluid. Therefore, the next step in the calculation is to expand the W_{nj} terms and to organize the resultant equations by collecting the $\zeta'_{a,n}$ and $\zeta'_{b,n}$ terms together. This results in two equations of the form

$$\eta_{a,n}\zeta'_{a,n} + \chi_{a,n}\zeta'_{b,n} = A\beta_a(\zeta'_{a,n-1} + \zeta'_{a,n+1}) \tag{41}$$

and

$$\eta_{b,n}\zeta'_{b,n} + \chi_{b,n}\zeta'_{a,n} = A\beta_b(\zeta'_{b,n-1} + \zeta'_{b,n+1}). \tag{42}$$

These equations can be cast as a single eigenvalue problem with $\zeta'_{a,n}$ and $\zeta'_{b,n}$ as the eigenvectors and A as the eigenvalue, taking the form

$$\begin{bmatrix}\eta_{a,n} & \chi_{a,n}\\ \chi_{b,n} & \eta_{b,n}\end{bmatrix}\begin{bmatrix}\zeta'_{a,n}\\ \zeta'_{b,n}\end{bmatrix} = A\begin{bmatrix}\beta_a & 0\\ 0 & \beta_b\end{bmatrix}\begin{bmatrix}\zeta'_{a,n-1} + \zeta'_{a,n+1}\\ \zeta'_{b,n-1} + \zeta'_{b,n+1}\end{bmatrix}. \tag{43}$$

The reality conditions for the ζ'_{-1} elements are given by $\zeta'_{-1} = \bar{\zeta}'_0$ and $\zeta'_{-1} = \bar{\zeta}'_1$ for subharmonic ($\alpha = \frac{\omega}{2}$) and harmonic ($\alpha = 0$) solutions, respectively, for both interfaces. This leads to implementation of a C matrix in order to couple the appropriate ζ' elements, which contains mostly ones and zeros. Since the reality conditions include the complex conjugates of ζ_n, Eq. (43) can again be decomposed into real and complex parts before solving, viz.,

$$\begin{bmatrix}\hat{\eta}_a & \hat{\chi}_a\\ \hat{\chi}_b & \hat{\eta}_b\end{bmatrix}\begin{bmatrix}\hat{\zeta}_a\\ \hat{\zeta}_b\end{bmatrix} = A\begin{bmatrix}\beta_a C & 0\\ 0 & \beta_b C\end{bmatrix}\begin{bmatrix}\hat{\zeta}_a\\ \hat{\zeta}_b\end{bmatrix}, \tag{44}$$

where $\hat{\zeta}_a$ and $\hat{\zeta}_b$ are column vectors of the form

$$\hat{\zeta}_a = \begin{bmatrix}\zeta'^r_{a,0}\\ \zeta'^i_{a,0}\\ \zeta'^r_{a,1}\\ \zeta'^i_{a,1}\\ \vdots\\ \vdots\\ \zeta'^r_{a,n-1}\\ \zeta'^i_{a,n-1}\\ \zeta'^r_{a,n}\\ \zeta'^i_{a,n}\end{bmatrix}, \tag{45}$$

$\hat{\eta}_a$, $\hat{\eta}_b$, $\hat{\chi}_a$, and $\hat{\eta}_a$ are all diagonal matrices which follow the form

$$\hat{\eta}_a = \begin{bmatrix} \hat{\eta}^r_{a,0} & -\hat{\eta}^i_{a,0} & 0 & 0 & 0 & 0 & 0 & 0 & 0 & 0 \\ \hat{\eta}^i_{a,0} & \hat{\eta}^r_{a,0} & 0 & 0 & 0 & 0 & 0 & 0 & 0 & 0 \\ 0 & 0 & \hat{\eta}^r_{a,1} & -\hat{\eta}^i_{a,1} & 0 & 0 & 0 & 0 & 0 & 0 \\ 0 & 0 & \hat{\eta}^i_{a,1} & \hat{\eta}^r_{a,1} & 0 & 0 & 0 & 0 & 0 & 0 \\ 0 & 0 & 0 & 0 & \ddots & \ddots & 0 & 0 & 0 & 0 \\ 0 & 0 & 0 & 0 & \ddots & \ddots & 0 & 0 & 0 & 0 \\ 0 & 0 & 0 & 0 & 0 & 0 & \hat{\eta}^r_{a,n-1} & -\hat{\eta}^i_{a,n-1} & 0 & 0 \\ 0 & 0 & 0 & 0 & 0 & 0 & \hat{\eta}^i_{a,n-1} & \hat{\eta}^r_{a,n-1} & 0 & 0 \\ 0 & 0 & 0 & 0 & 0 & 0 & 0 & 0 & \hat{\eta}^r_{a,n} & -\hat{\eta}^i_{a,n} \\ 0 & 0 & 0 & 0 & 0 & 0 & 0 & 0 & \hat{\eta}^i_{a,n} & \hat{\eta}^r_{a,n} \end{bmatrix}, \tag{46}$$

and the C matrix takes the form (for $\alpha = \frac{\omega}{2}$)

$$C = \begin{bmatrix} 1 & 0 & 1 & 0 & 0 & 0 & 0 & 0 & 0 & 0 \\ 0 & -1 & 0 & 1 & 0 & 0 & 0 & 0 & 0 & 0 \\ 1 & 0 & 0 & 0 & 1 & 0 & 0 & 0 & 0 & 0 \\ 0 & 1 & 0 & 0 & 0 & 1 & 0 & 0 & 0 & 0 \\ 0 & 0 & \ddots & 0 & 0 & 0 & \ddots & 0 & 0 & 0 \\ 0 & 0 & 0 & \ddots & 0 & 0 & 0 & \ddots & 0 & 0 \\ 0 & 0 & 0 & 0 & 1 & 0 & 0 & 0 & 1 & 0 \\ 0 & 0 & 0 & 0 & 0 & 1 & 0 & 0 & 0 & 1 \\ 0 & 0 & 0 & 0 & 0 & 0 & 1 & 0 & 0 & 0 \\ 0 & 0 & 0 & 0 & 0 & 0 & 0 & 1 & 0 & 0 \end{bmatrix} \tag{47}$$

or (for $\alpha = 0$)

$$C = \begin{bmatrix} 0 & 0 & 2 & 0 & 0 & 0 & 0 & 0 & 0 & 0 \\ 0 & 0 & 0 & 0 & 0 & 0 & 0 & 0 & 0 & 0 \\ 1 & 0 & 0 & 0 & 1 & 0 & 0 & 0 & 0 & 0 \\ 0 & 1 & 0 & 0 & 0 & 1 & 0 & 0 & 0 & 0 \\ 0 & 0 & \ddots & 0 & 0 & 0 & \ddots & 0 & 0 & 0 \\ 0 & 0 & 0 & \ddots & 0 & 0 & 0 & \ddots & 0 & 0 \\ 0 & 0 & 0 & 0 & 1 & 0 & 0 & 0 & 1 & 0 \\ 0 & 0 & 0 & 0 & 0 & 1 & 0 & 0 & 0 & 1 \\ 0 & 0 & 0 & 0 & 0 & 0 & 1 & 0 & 0 & 0 \\ 0 & 0 & 0 & 0 & 0 & 0 & 0 & 1 & 0 & 0 \end{bmatrix}, \tag{48}$$

where n is the Fourier series cutoff. After constructing the matrices, the growth rate σ is set to 0 and the eigenvalue problem is solved computationally, yielding a set of eigenvalues and eigenvectors. The lowest real eigenvalue of this set is that which governs the stability of the system, and its corresponding eigenvector gives the relative deflection between the top and bottom interfaces. This threshold eigenvalue corresponds to the amplitude where the instability first manifests when slowly raising the amplitude of oscillation at a given forcing frequency.

Thus far, the system has been taken to be laterally unbounded. In order to constrain the system to a particular geometry, the tested wave numbers are constrained to only those that form 90° angles with the sidewalls, as outlined by Benjamin and Ursell [7]. For the cylindrical geometries of interest

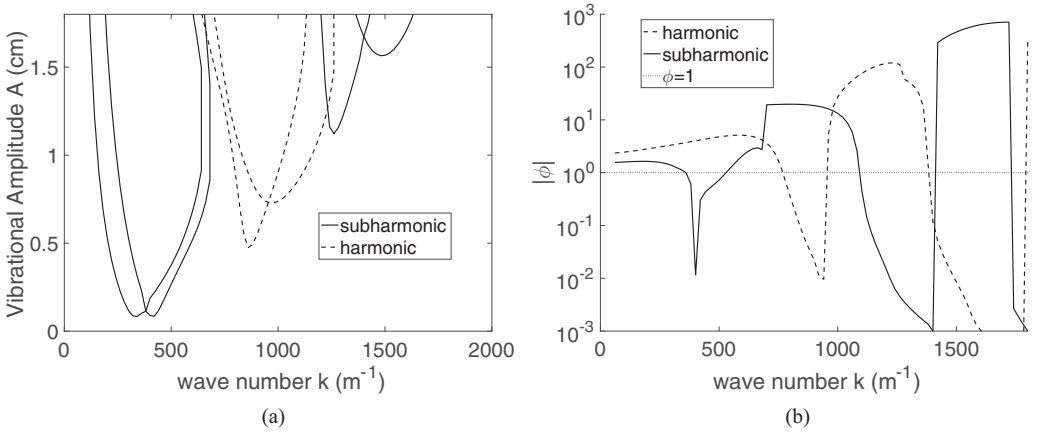

FIG. 2. Predicted stability curve and relative interfacial deflections for a three-fluid mechanically forced system. (a) Theoretical predictions for critical amplitudes utilizing the fluid combination summarized in Table I. Double-tongued stability curves are observed for three-fluid Faraday instability systems, where each section of a tongue is dominated by one of the interfaces. The testing frequency is 9 Hz. (b) Relative interfacial deflection ϕ vs wave number. Here $\phi = 1$ indicates a comparable deflection of the interfaces, $\phi < 1$ indicates higher deflection on the top interface, and $\phi > 1$ indicates higher deflection on the bottom interface. For example, for $k = 250$ m^{-1}, the subharmonic and harmonic tongues in (a) indicate that the bottom interface has the higher deflection and at $k = 500$ m^{-1}, the upper interface has the higher deflection for the subharmonic tongue while the reverse is true for the harmonic tongue. Note that the harmonic tongues at $k = 250$ and 500 m^{-1} appear at very large vibrational amplitudes not depicted within the scale of (a).

to the present work, these wave numbers are given by those that satisfy

$$\left(\frac{\partial^2}{\partial r^2} + \frac{1}{r}\frac{\partial}{\partial r} + \frac{1}{r^2}\frac{\partial}{\partial \theta} + k_m^2\right)\zeta_m = 0 \tag{49}$$

subject to $\frac{\partial \zeta_m}{\partial r} = 0$ at $r = R$, the solution of which shows that $k_{l,m}R$ is given by the mth root of $J_l'(r)$, where l and m are the numbers of azimuthal nodes and radial nodes, respectively.

The final stability curve for a constrained geometry with stress-free sidewalls is calculated by solving Eq. (44) for all the allowable wave numbers, typically truncated at $l = m = 5$, and a given frequency. The resultant lowest eigenvalues for each wave number are compared and the lowest of all is selected as the threshold amplitude for the tested frequency. The harmonicity and waveform at the onset are given by the wave number and α which produced this threshold amplitude. The calculation is then repeated over a large frequency range to generate the final stability curve of A versus ω for comparison to experiments. As mentioned earlier, all calculations in this study are reported unscaled in order to give a physical sense of dimensions and the thresholds.

III. RESULTS FROM THEORY

A. Stability thresholds and relative interfacial deflections

To relate the three-fluid mechanically forced Faraday instability to the well-known two-fluid case, the stability curves for an unbounded geometry are first examined. Figure 2(a) shows a plot of amplitude versus wave number for a fluid set with properties summarized in Table I.

As can be seen in Fig. 2(a), double-tongued stability curves are observed for three-fluid systems. This is in direct contrast to the single tongues observed in two-fluid systems [7]. The reader should note that the second lowest eigenvalue is also plotted inside each tongue in Fig. 2(a) to show the separate eigenvalue branches responsible for the double minimum. Though the tongues exhibit

TABLE I. Fluid properties for the generation of Fig. 2. These fluids and heights were chosen to highlight the double tongues that can be obtained when parametrically forcing a three-fluid system.

Fluid	Density ($\mathrm{kg\,m^{-3}}$)	Kinematic viscosity (cSt)	Layer height (mm)	Interfacial tension ($\mathrm{N\,m^{-1}}$)
A	856	1.5	5	$0.007 = \gamma_a$
B	1200	1.0	5	$0.007 = \gamma_b$
C	1880	14	5	

a double minimum for this fluid system, they retain the typical behavior of alternating between subharmonic and harmonic seen in the two-fluid case. On any particular tongue, multiple regions can be found: those at which one interface dominates the stability of the overall system, those where the opposite interface dominates, and those where both interfaces contribute relatively the same amount. This may be seen by examining the relative interfacial deflections of the interfaces as a function of wave number [Fig. 2(b)]. For the purposes of this illustration, the amplitude of the interfacial deflection of each interface and the relative deflection are calculated using the formulas [from Eq. (16)]

$$\bar{\zeta}_a = \sum_{n=0}^{N} \zeta'_{a,n} e^{i(\alpha+n\omega)},$$
$$\bar{\zeta}_b = \sum_{n=0}^{N} \zeta'_{b,n} e^{i(\alpha+n\omega)}, \tag{50}$$

and

$$\phi = \frac{\bar{\zeta}_a}{\bar{\zeta}_b}. \tag{51}$$

The highest and lowest regions of relative interfacial deflection typically occur just before two eigenvalue branches intersect, while the point where they intersect corresponds to a relative deflection of precisely unity, denoting that the deflection ought to be comparable at both interfaces. Though the two interfaces have differing relative deflections, it is important to note that linear stability analysis results in only one critical amplitude for a given wave number and implies that both interfaces become unstable simultaneously. Practically, however, if the relative deflection is very large or very small, one interface may appear to be nearly flat while the other obviously deflects substantially.

Figure 3(a) shows the effect of middle fluid viscosity on the system stability. As expected, the trend follows that of the two-fluid case, i.e., increased viscosity causes a shifting of the tongues to higher wave number and higher critical amplitude. This behavior can cause interesting consequences when the viscosity of the top or bottom fluid is adjusted, however, as shown in Fig. 3(b). Perhaps not surprisingly, when either the top or bottom fluid has a much higher viscosity than the other two fluids, one eigenvalue branch is shifted much more than the other. In extreme cases this can result in a single-tongued stability curve again, with the tongues stemming only from the eigenvalue branches where the relative deflection favors the interface not in immediate contact with the viscous fluid. This occurs when the eigenvalue branch related to the interface in contact with the more viscous fluid has a threshold much higher than the other eigenvalue branch, causing the lowest critical amplitude to always be that which is found on the branch related to the interface comprised of the less viscous fluid pair. Both complete eigenvalue branches are shown for clarity, though the lowest one at a given wave number is the one that governs the system stability.

Figure 4 shows the effect of increasing frequency on the system stability. Again, this behavior follows closely that observed for a two-fluid case. An increase in frequency causes the tongues to

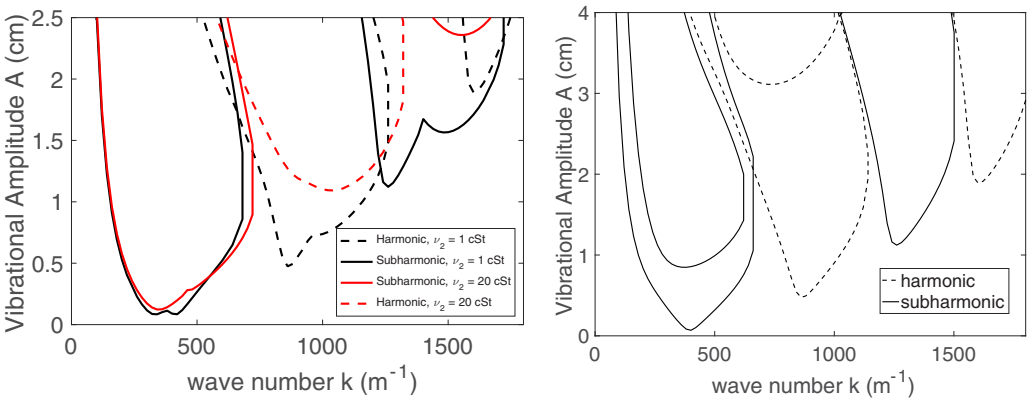

(a) (b)

FIG. 3. Effect of viscosity on three-fluid instability thresholds. (a) The black lines are obtained using the fluid properties summarized in Table I, while the red lines are obtained by increasing the viscosity of the middle fluid by a factor of 20. As predicted, increasing the middle fluid viscosity causes a shift of the threshold to higher amplitude and higher wave number. The testing frequency is 10 Hz. (b) Effect obtained when the top or bottom fluid is much more viscous than the other two. The testing frequency is 9 Hz. The fluid properties are the same as those shown in Table I with the exception of ν_1, which is set at 120 cSt.

shift down in amplitude and to higher wave number. In a constrained geometry, this would cause the system to access higher-wave-number modes with increasing frequency, with the threshold becoming lower with increasing frequency.

B. Comparison to the single-interface problem

As can be inferred from the tanh(kh) term found in Ref. [7], once the height of the middle fluid becomes high enough, the interfaces no longer interact with one another. This can be seen by

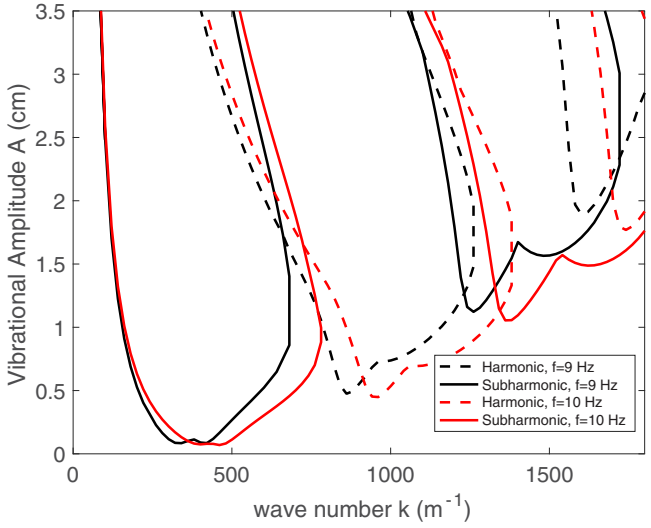

FIG. 4. Effect of increasing frequency on the stability of the system. In general, an increase in frequency causes the tongues to shift to higher wave number and lower amplitude. The fluid properties are those shown in Table I.

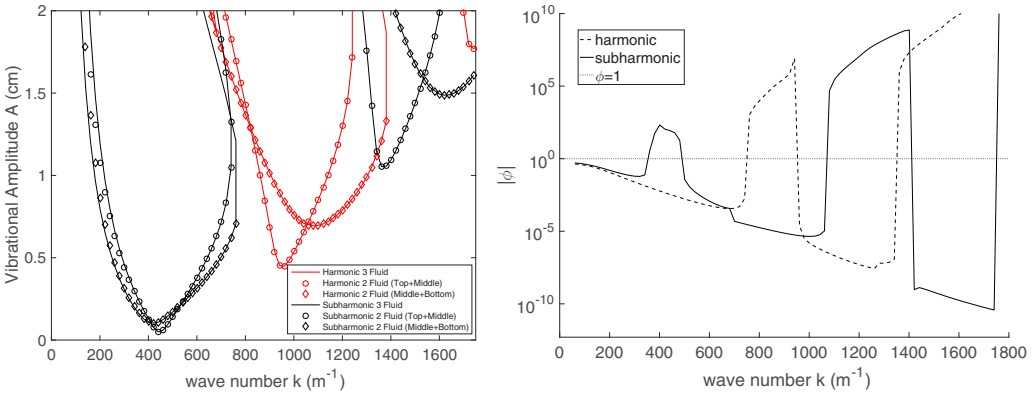

FIG. 5. Comparison between the three-fluid stability thresholds and the corresponding two-fluid cases for tall middle fluid heights. (a) Three-fluid calculation versus corresponding two-fluid calculations for high middle fluid heights. The properties are those shown in Table I and layer heights are 0.5 cm for the bottom, 1 cm for the middle, and 0.5 cm for the top. Solid lines show the three-fluid stability curve prediction and symbols show the corresponding top-middle fluid and middle-bottom fluid two-fluid calculations. The agreement between the tongues generated by the separate two-fluid calculations and the three-fluid calculation is excellent, with the only discrepancies occurring at low wave number. (b) Relative deflection versus wave number for the tall middle fluid system. The relative deflection can be accurately predicted by determining which eigenvalue branch occurs at lower amplitude in (a).

conducting three separate calculations, the first of which is the three-fluid case with a tall middle layer. The other two calculations are done for corresponding two-fluid systems, one supposing that the initial bottom fluid is replaced with more middle fluid and the other supposing that the initial top fluid is replaced with more middle fluid. The results of these calculations is shown in Fig. 5(a). As expected, the three-fluid stability curve is composed almost exactly of the two separate two-fluid cases. The only exception occurs at low wave number, where $\tanh(kh)$ has not yet saturated and the interfaces still influence one another. This calculation shows that the system behaves almost identically to two separate two-fluid systems when the middle height is large enough. In addition, Fig. 5(b) shows the relative interfacial deflections with this fluid height. It can be seen that now, the lowest eigenvalue branch directly correlates to the relative interfacial deflections. Therefore, it can be inferred that each eigenvalue branch is produced almost solely due to contributions from the fluid pair comprising a single interface.

Interestingly, the opposite does not hold true when the height of the middle layer is very small. In this case, the system does exhibit stability tongues with a single minimum, but the stability thresholds do not match that of the two-fluid system between the top and bottom fluids. A comparison between the two cases is shown in Fig. 6(a). As can be seen clearly from the comparison, the effect of the minuscule third fluid layer can have both stabilizing and destabilizing effects on the system. On this single minimum stability curve, the relative deflection approaches unity for all wave numbers as the middle fluid height decreases for the subharmonic tongues. However, the harmonic tongues do not exhibit the same behavior. In their case, the interface with the larger $\Delta\rho$ always deflects more than the other and thus the relative deflection is always greater than or less than unity across all wave numbers. This is shown in Fig. 6(b), and a companion calculation with $(\Delta\rho)_a = (\Delta\rho)_b$ is shown in Fig. 6(d) to show that this behavior is related to bias caused by the $\Delta\rho$ imbalances.

Adding a third fluid at the top or bottom of a two-fluid system can also cause dramatic changes to the stability of the system, allowing for selective destabilization or stabilization to particular waveforms at a given frequency. Figure 7 shows an example of this behavior by comparing a

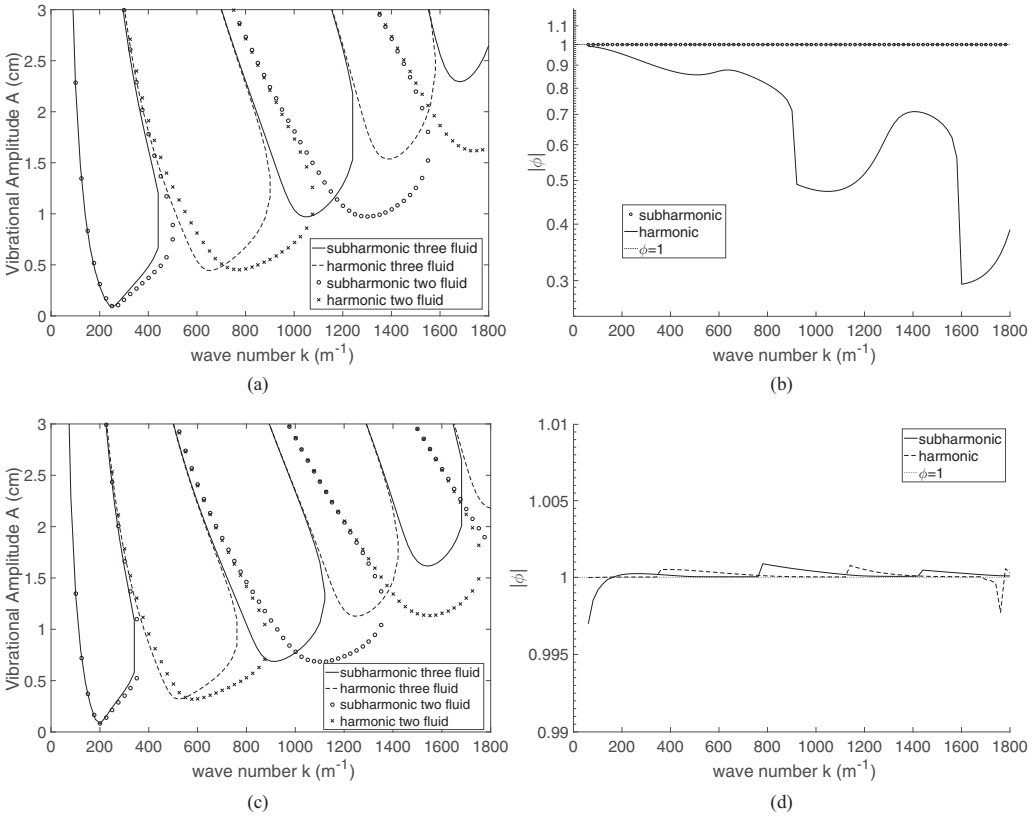

FIG. 6. Comparison between the three-fluid stability thresholds and the corresponding two-fluid cases for short middle fluid heights. (a) The properties are those shown in Table I and the layer heights are 0.5 cm for the bottom, 0.000 01 cm for the middle, and 0.5 cm for the top. Solid lines show the three-fluid stability curve prediction and symbols show the corresponding top-bottom two-fluid calculation with an assumed interfacial tension of $\gamma = \gamma_a = \gamma_b$. The two different predictions agree only at low wave number and differ dramatically with increasing wave number. (b) Relative deflection versus wave number for the short middle fluid system. The relative deflection approaches unity for the subharmonic tongues, but always favors the interface with the higher $\Delta\rho$ for the harmonic tongues. (c) Three-fluid small middle height calculation versus the corresponding two-fluid calculation with no density difference bias. The fluid properties are the same as in (a), but with $\rho_3 = 520\ \mathrm{kg\,m^{-3}}$. (d) Relative deflection for nonbiased three-fluid system. Here ϕ approaches unity for both harmonic and subharmonic responses in the absence of a $\Delta\rho$ bias.

two-fluid system with a set total height to a corresponding three-fluid system in which the third fluid replaces half of the height of the former top fluid. In this system, regions of both destabilization (e.g., $k = 85$–$310\ \mathrm{m^{-1}}$) and stabilization (e.g., $k = 60$–$85\ \mathrm{m^{-1}}$) can be obtained through the addition of the third fluid. By changing the properties of the additional fluid, the zones of stabilization and destabilization could potentially be tailored for a given application in order to more efficiently utilize or suppress the Faraday instability for process enhancement.

Another interesting phenomenon that arises within three-fluid systems stems from the fact that two-fluid systems can only become Faraday unstable if there is a finite density difference between the two fluids. This can be seen by looking at the final stress balance equation. If the fluid pair has a small density difference, $\Delta\rho$ appearing in the $A\Delta\rho$ term seen in Eq. (40), say, will become very small and thus the critical amplitude A will become very large. As a result, the stability threshold in such a two-fluid system is almost unattainable experimentally. The destabilization arising from the

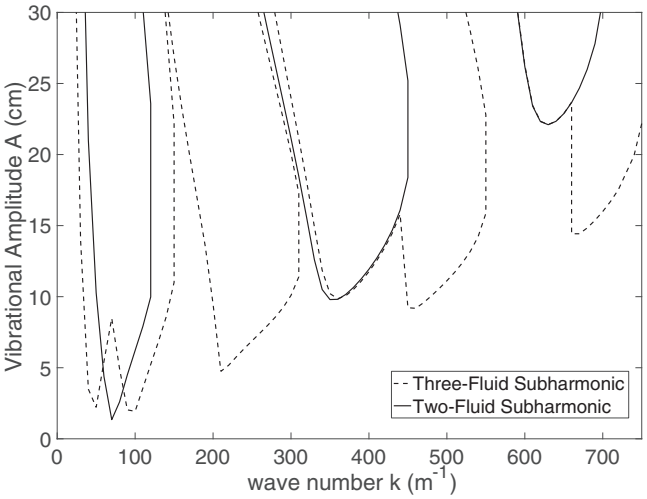

FIG. 7. Comparison between the stability thresholds for a two-fluid case and a three-fluid case with the same total height where the third fluid is added at the top. The forcing frequency ω is 2 Hz. The fluid parameters for the two-fluid case are $\rho_1 = 1000\ \mathrm{kg\,m^{-3}}$, $\nu_1 = 12$ cSt, $h_1 = 1.27$ cm, $\rho_2 = 846\ \mathrm{kg\,m^{-3}}$, $\nu_2 = 1.5$ cSt, $h_2 = 1.27$ cm, and $\gamma = 0.007\ \mathrm{kg\,m^{-2}}$. The fluid parameters for the three-fluid case are $\rho_1 = 1000\ \mathrm{kg\,m^{-3}}$, $\nu_1 = 12$ cSt, $h_1 = 1.27$ cm, $\rho_2 = 846\ \mathrm{kg\,m^{-3}}$, $\nu_2 = 1.5$ cSt, $h_2 = 0.635$ cm, $\rho_3 = 600\ \mathrm{kg\,m^{-3}}$, $\nu_3 = 1$ cSt, $h_3 = 0.635$ cm, and $\gamma_a = \gamma_b = 0.007\ \mathrm{kg\,m^{-2}}$. Multiple regions of stabilization and destabilization can be observed. Harmonic solutions are omitted for clarity.

addition of a third fluid, however, can alleviate this problem if one seeks to destabilize an interface with a small $\Delta\rho$ or even one with a $\Delta\rho$ of exactly zero. A demonstration of this is shown in Fig. 8. In this case, the fluid parameters are taken to be that described in Table I, with the exception that the middle fluid's density is adjusted to $\rho_2 = \rho_1 = 1880\ \mathrm{kg\,m^{-3}}$.

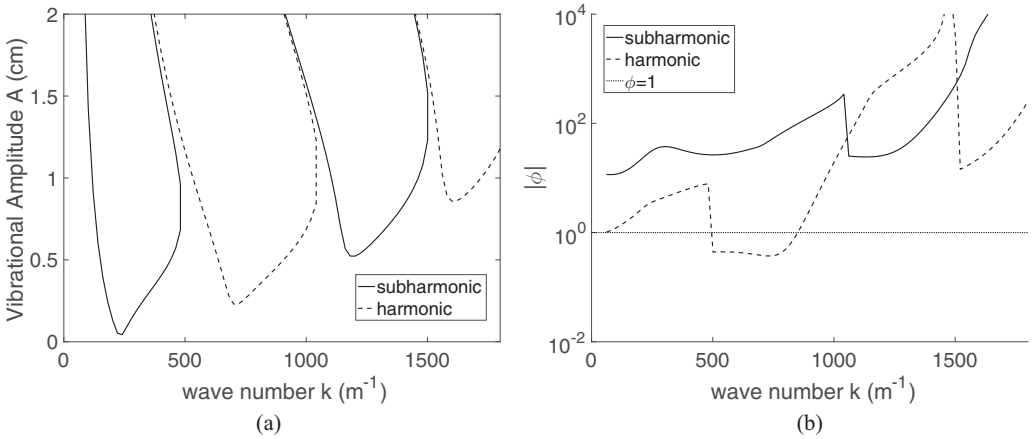

FIG. 8. Three-fluid stability curve with one interface containing $\Delta\rho = 0$. (a) Stability curve for the fluids described in Table I with ρ_2 set to 1880 $\mathrm{kg\,m^{-3}}$, therefore making $\Delta\rho_b$ equal to 0. The testing frequency is 9 Hz. (b) Relative deflections of the instability at onset versus wave number. A wave-number range at which the bottom interface deflects more than the top interface can be seen, even though its $\Delta\rho$ is zero.

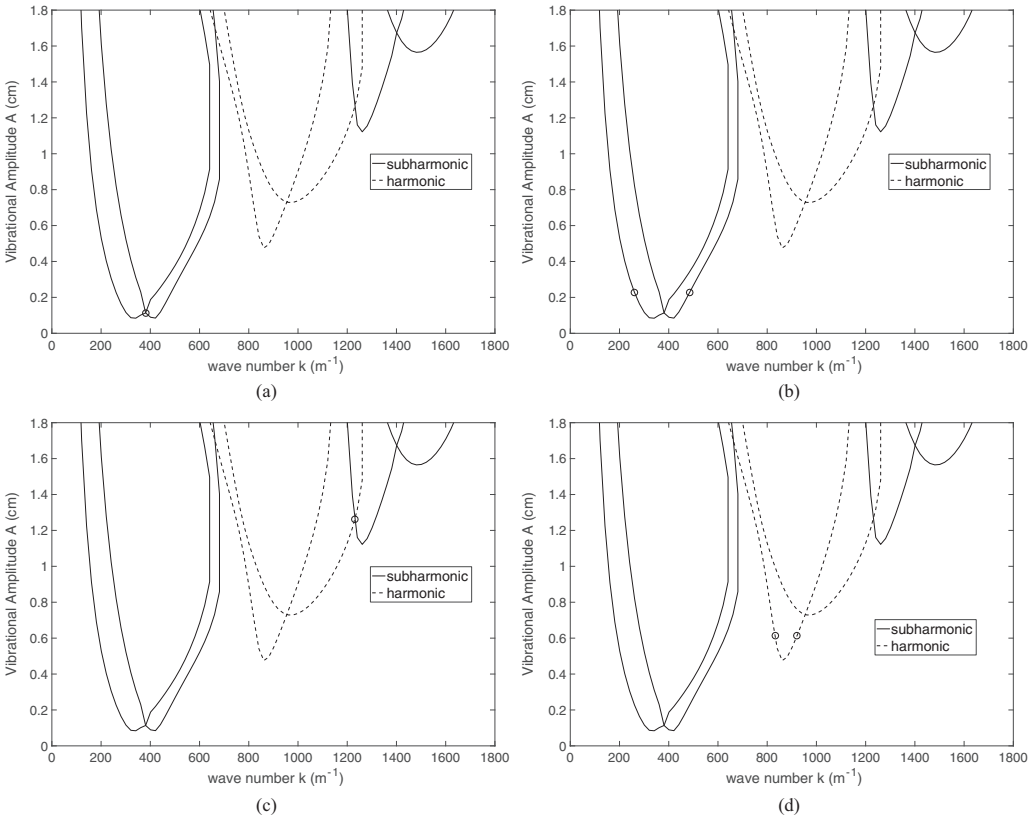

FIG. 9. Four possible codimension points obtainable in the three-fluid mechanically forced Faraday instability. (a) Codimension point where relative deflection between the interfaces is equal to 1. At this point, both interfaces will become unstable simultaneously with comparable interfacial deflections. (b) Codimension point between tongues with opposing relative interfacial deflections, resulting in mode expressions that are biased on each interface based upon the relative deflections. (c) Codimension point for a single mode at multiple harmonicities. This type of point is unachievable in two-fluid systems because the harmonic and subharmonic tongues never meet. (d) Example of the type of codimension point achievable in two-fluid systems. One eigenvalue branch exhibits the same critical amplitudes for multiple wave numbers, resulting in a codimension point. This can also be achieved for multiple wave numbers at different harmonicities.

As can be observed, the system is able to produce stability curves even with the $\Delta\rho_b$ set to zero. Since the stability curves in this case present with a single minimum, it is intuitive that these curves occur almost solely due to the interface with a nonzero $\Delta\rho$ and thus it will always have a much higher deflection than the other. However, by examining the relative deflection versus wave-number plot shown in Fig. 8(b), it can clearly be seen that a wave-number range does exist in which $\zeta_b \geqslant \zeta_a$. Thus, if a geometry was selected such that the wave number with the lowest critical amplitude fell within this range, the interface with a $\Delta\rho$ of zero would exhibit instability with a non-negligible deflection, directly contrary to the case with only two fluids.

C. Codimension points obtainable in the three-fluid system

Since the instability tongues actually stem from two distinct eigenvalue branches, codimension points that are unattainable in two-fluid cases can be observed upon the addition of a third fluid. Figure 9 shows three examples of this type of codimension point.

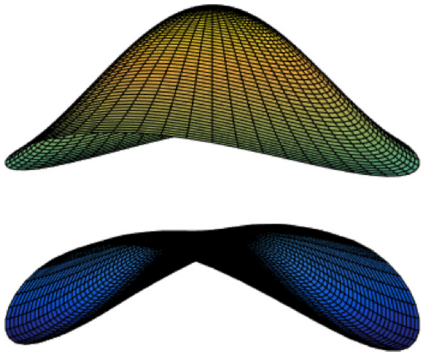

FIG. 10. Theoretical waveform representation for competing (0,1) and (2,1) modes. The top interface exhibits a mode which is primarily (0,1), while the bottom interface exhibits a mode which is primarily (2,1).

The first type of codimension point, shown in Fig. 9(a), is that where the relative deflection is equal to unity. This type of codimension point corresponds to a wave number which has interesting properties. At this point, the two interfaces would tend to become unstable with comparable relative deflections. However, the portion of the tongue at slightly lower wave number exhibits a positive slope, while the portion of the tongue at slightly higher wave number exhibits a negative slope. Though linear stability analysis does not offer any insight into the temporal evolution of the interface after the onset of the instability, previous studies in two-fluid systems [13,24,25] have shown that performing experiments within the zones of negative slope on an A vs ω plot (i.e., a positive slope on an A vs k plot) experimentally yields subcritical bifurcations, while conducting experiments in zones of positive slope on an A vs ω plot (i.e., a negative slope on an A vs k plot) experimentally yields supercritical bifurcations. This phenomenon was observed by experimentally monitoring the temporal evolution of the interface over the course of an experiment after exciting the instability near the threshold. Therefore, assuming that the typically observed trend holds true, the eigenvalue branch for one interface yields an instability which will tend to exhibit a subcritical bifurcation, while the other interface will tend to exhibit a supercritical bifurcation. This point can be seen as one where the two interfaces would both tend to be unstable with the same mode and harmonicity, but one interface would likely bifurcate subcritically while the other would likely bifurcate supercritically. The dominant bifurcation, however, is undetermined via the present analysis. Experimentally, as can be inferred through Fig. 4, this would cause a single mode to appear first subcritically, then supercritically, then subcritically again, and finally supercritically before transitioning to another mode when increasing frequency. This type of behavior is unobtainable in a two-fluid system, as the single stability tongues only possess one minimum.

The second type of codimension point, as shown in Fig. 9(b), is obtained when two wave numbers have the same critical amplitude but lie on parts of their respective tongues with opposing relative deflections. In other words, one interface would tend to become unstable with one mode, while the other interface would tend to become unstable with a completely different mode. The resultant waveform, from a linear instability perspective, would be a combination of the two modes. However, it is possible that one interface would exhibit a combination which preferentially favors one mode, while the other interface exhibits the opposite combination. A pictorial representation of this possibility is shown in Fig. 10, where both interfaces exhibit a combination of (2,1) and (0,1) modes. The top interface adopts a dominant (0,1) waveform, while the bottom interface adopts a dominant (2,1) waveform.

Codimension points for a single wave number at different harmonicities can also be obtained, as shown in Fig. 9(c). This type of codimension point is unattainable in two-fluid systems because in these systems the subharmonic and harmonic tongues never intersect. This type of behavior is also seen in the three-fluid case between eigenvalue branches of equivalent relative deflection. For

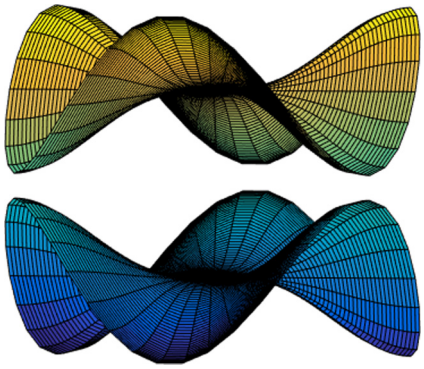

FIG. 11. Theoretical waveform representation for two out-of-phase (3,1) modes. Both interfaces exhibit comparable relative deflection, yet their waveforms appear out of phase with one another.

example, a harmonic top-interface-dominated branch will never intersect with a subharmonic top-interface-dominated branch. However, a top-dominated subharmonic branch can intersect with a bottom-dominated harmonic branch, allowing for the presence of these types of codimension point. This type of point would presumably manifest with both interfaces exhibiting the same waveform but different harmonicities at the onset of the instability.

In addition to these types of codimension points, the three-fluid system can also exhibit the codimension points present in the two-fluid case. Namely, these occur when two wave numbers on the same type of eigenvalue branch exhibit the same critical amplitude, resulting in a competition between two distinct modal structures of the same or different harmonicities. The relative deflections at both wave numbers are comparable and far away from unity, meaning that the mode will primarily show on one of the two interfaces. This type of codimension point is shown in Fig. 9(d).

Another interesting phenomenon that can occur when utilizing two-fluid systems is the expression of the instability on both interfaces simultaneously but out of phase. A theoretical example of this type of behavior is shown in Fig. 11. In this case, the top and bottom interfaces are both exhibiting (3,1) modes with comparable relative deflections, but precisely out of phase with one another. This is indicated by the calculation when the relative deflection value, before taking the absolute value, yields a negative number, as shown in Fig. 12. This typically occurs only at extreme values of the relative deflection, i.e., $|\phi| \ll 1$ or $|\phi| \gg 1$. To depict some of the observations made through calculations, we turn to an experiment, describing the method and the reasons for the fluids of choice, and then conclude with a comparison to the theoretical model.

IV. EXPERIMENTAL METHOD

Finding fluid choices for experimental validation of the model posed great difficulty. In particular, all three fluids needed to be immiscible to avoid unintentional mixing during filling of the cell or during excitation of a subcritical instability. In addition, an ideal fluid combination would exhibit low stress at the sidewall in order to uphold the sidewall assumption present in the model. Previous experiments by Batson *et al.* [13] utilized 1.5-cSt silicone oil and FC-70 to effectively achieve this goal and obtain superb agreement with theory. These two fluids were thus selected as two of the fluids in the present work. After much experimentation, it was decided to use ultrapure water as the third fluid, in this case the middle fluid. It might be noted that the value of the interfacial tension plays a negligible role in the determination of the critical amplitude, an observation made by earlier workers [8], thus any minor impurities that might migrate to the aqueous interface would have no consequence on the instability threshold.

The cell which contained water was found to produce a meniscus on both interfaces which pointed down into the FC-70 and up into the silicone oil due to the tendency of the water to wet

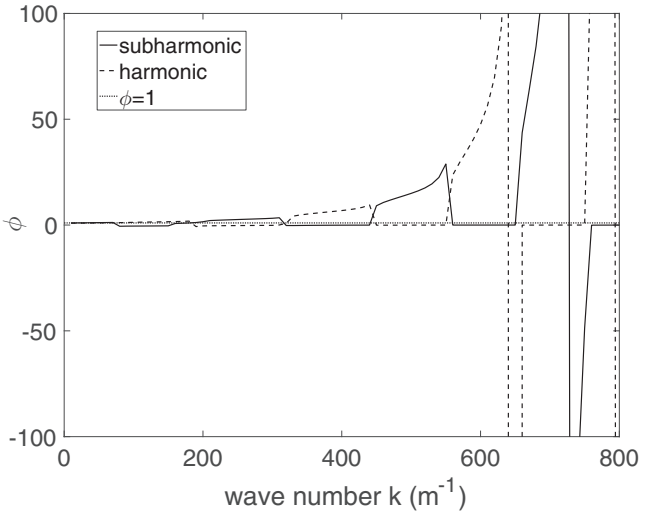

FIG. 12. Relative deflection before taking the absolute value for the three-fluid system described in Fig. 7 versus wave number. The relative deflection is negative at various wave numbers. However, the negative values typically occur when $|\phi| \ll 1$ or $|\phi| \gg 1$.

the glass sidewalls. These menisci caused imperfections in the experiment in the form of meniscus waves that were harmonic in nature and axisymmetric. However, these types of waves were found previously to only affect the (0,1) harmonic mode onset [13]. Though the sidewall behavior of this system was not ideal, it was chosen as the system to be used for the validation experiments due to the lack of a superior fluid combination. Table II summarizes the fluid properties of the system.

The tested geometries were a 5.08-cm-diam cylinder with an overall height of 6.4 cm and a 12.7-cm-diam cylinder with an overall height of 5.08 cm. The smaller geometry was tested due to the excellent agreement obtained by Batson *et al.* [13] when utilizing the same geometry in two-fluid experiments and the larger was tested in order to minimize sidewall effects. Both cylinders were cut from commercially available glass piping and were contained between acrylic top and bottom plates. The choice of glass for the sidewalls was made due to discrepancies observed in previous experiments when utilizing acrylic sidewalls. In fact, the stress-free sidewall condition was experimentally simulated by utilizing fluids in which the less viscous fluid predominately wets the sidewalls, allowing the interface to slide easily as if the system were stress free. In the case of glass sidewalls, the wetting behavior of the silicone oil and FC-70 system utilized by Batson *et al.* [13] met these conditions. When the same experiments were conducted using acrylic sidewalls, the FC-70 began to wet the walls and thus the stress-free sidewall assumption was not upheld. The top and bottom walls, however, were presumed to have negligible effect on the instability thresholds due to their distance from the interfaces and thus acrylic was chosen due to ease of fabrication. For practical experiments, the height of the middle layer needed to be large enough to be visible

TABLE II. Fluid properties for silicone oil, water, and FC-70. Densities and interfacial tensions were measured and viscosities were assumed to be that labeled on the bottle.

Fluid	Density (kg m^{-3})	Kinematic viscosity (cSt)	Interfacial tension (N m^{-1})
silicone oil	825	1.5	$0.045 = \gamma_a$
water	1000	1.0	$0.051 = \gamma_b$
FC-70	1940	14	

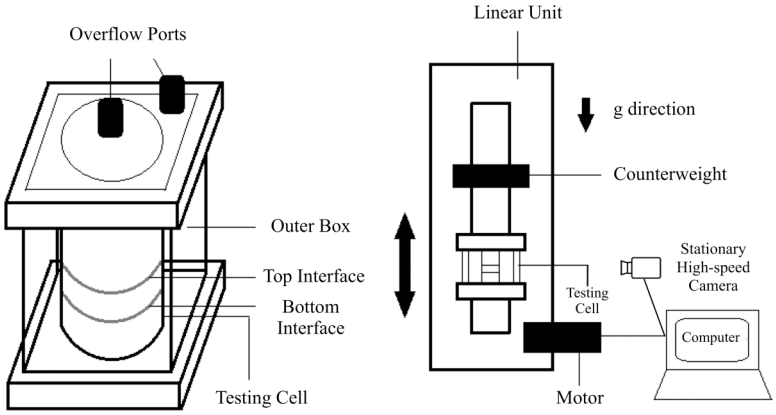

FIG. 13. Assembled testing cell and experimental setup. The base plate attaches to the mechanical shaker and is secured with four screws. Backlighting allows for the clear visualization of the interface and any deflection using a high-speed camera.

yet small enough to retain the coupling between the interfaces. In addition, a minimum amount of water was necessary to create an actual fluid layer, any less of which would cause beading of the water preferentially on the sidewalls and a bridge between the silicone oil and FC-70 in the center of the testing cell. This led to an ideal fluid height of 1.68 cm of water, with the balance split evenly between silicone oil and FC-70 (2.36 cm each) for the smaller cylinder. Heights of 2.01, 1.5, and 1.63 cm for the FC-70, water, and silicone oil, respectively, were utilized in the larger geometry.

The filling procedure for the testing cell first involved a thorough cleaning of the cell with water and isopropanol before drying with compressed air to minimize contaminants on the surfaces in contact with the fluid. The cell was then assembled and sealed via compression using wing nuts and Buna-N rubber gaskets, which did not interact or swell when exposed to any of the testing fluids. Fluids were then filled by density from highest to lowest through a small hole in the top of the cell connected to an overflow port. This port served to contain extra silicone oil as well as free space to accommodate for the expansion and contraction of the fluids due to temperature changes in the room, allowing for long-term use of the same testing fluids without generation of air bubbles within the cell. A rectangular outer bath was also filled with water around the testing cell to combat the image distortion caused by the curvature of the glass. Finally, a grid was affixed to the back of the cell to aid in imaging and a small white sheet of paper with a thin black line was attached to the cell to aid in the determination of the exact frequency and amplitude with which the cell was shaking through image analysis. Figure 13 shows a schematic of the assembled testing cell and mechanical shaker apparatus.

After filling, the assembled testing cell was mounted to the mechanical shaker, leveled, and secured using four screws through a metal base plate. The cell was backlit using a light mounted to the shaker for visualization which moved with the testing cell and recordings were taken using a stationary high-speed camera. The mechanical shaker was controlled externally using a computer program, allowing the user to input a frequency and amplitude of oscillation. This input was found to be accurate for the frequency of oscillation, but the actual amplitude of oscillation of the cell varied from that which was imposed. This warranted the conduction of image analysis on each experimental run to determine the actual oscillation amplitude accurate to within one pixel (2% error in the amplitude or better).

During the course of the experiments, a frequency of oscillation was first chosen for a given test. An amplitude higher than the theoretical threshold was then input and the shaker was made to oscillate in order to observe the instability. Subsequent runs decreased the amplitude of oscillation while keeping the frequency constant, until the system remained stable for a period of 3 min after

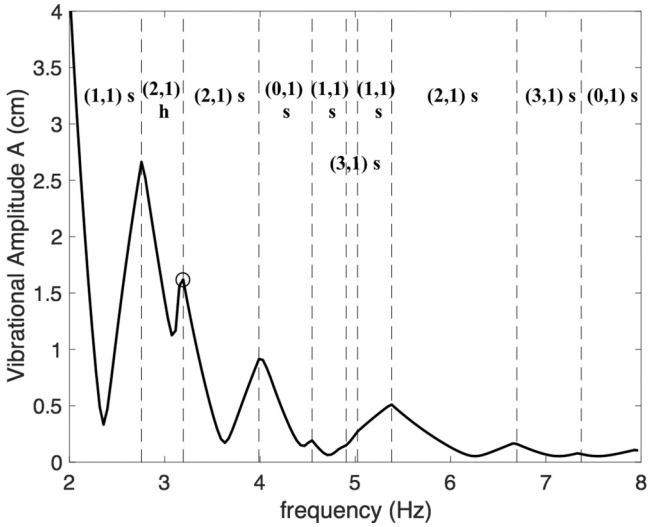

FIG. 14. Theoretical amplitude versus frequency plot for the three-fluid system described by Table II. The black circled point is an example of a three-fluid exclusive codimension point shown in Fig. 9(c). Distinct modes are enclosed between pairs of dashed lines and labeled, with an s denoting a subharmonic response and an h denoting a harmonic response.

starting the forcing. For the purposes of the present work, stability was defined by the absence of any observable Faraday waves on either interface. The experimental threshold was determined by narrowing down the imposed amplitudes which resulted in a stable and unstable system until a suitable precision was reached, typically 0.1 or 0.2 mm. At this point, the experimental threshold was determined to be the midpoint between the nearest stable and unstable tested amplitudes. The threshold was recorded, along with the resultant waveform, qualitative relative deflections at the onset, and harmonicity of the response before moving to a new oscillation frequency and repeating the process.

V. RESULTS FROM EXPERIMENTS

Figure 14 shows the theoretically produced stability curves for the system described by Table II when utilizing the 5.08-cm-diam cylinder. The predicted modes and harmonicities are enclosed between pairs of dashed lines and labeled accordingly. Before showing experimental data, it is important to note several differences between this A vs ω plot and the typical two-fluid plot of this kind. Since there are two interfaces, modes are able to repeat themselves at the same harmonicity in different frequency bands. This can be observed in Fig. 14 by the repeated $(2, 1)_s$, $(3, 1)_s$, and $(0, 1)_s$ regions. The black circled point shows an example of the type of codimension point mentioned in Fig. 9(c), which is also unattainable in two-fluid systems. Finally, interesting behavior can be observed in the (4.5–5.5)-Hz region, where a $(3, 1)_s$ tongue appears seemingly within a $(1, 1)_s$ tongue. This behavior happens due to the double-minimum stability behavior, as the $(3, 1)_s$ tongue is occurring on a distinct eigenvalue branch from the $(1, 1)_s$ tongue, allowing it to interfere with the natural smooth occurrence of the $(1, 1)_s$.

Figure 15 compares the theoretical results with experiments conducted using the system described in Table II and the 5.08-cm-diam geometry. Since the experimental system did not precisely honor the stress-free sidewall assumption present in the model, a shift in the tongues to higher frequency occurs, causing discrepancy between the theory and the experiment. Qualitatively, however, it can be seen that the mode order of appearance with increasing frequency is correctly predicted by the theory for all modes except the $(0, 1)_h$ mode observed experimentally in the

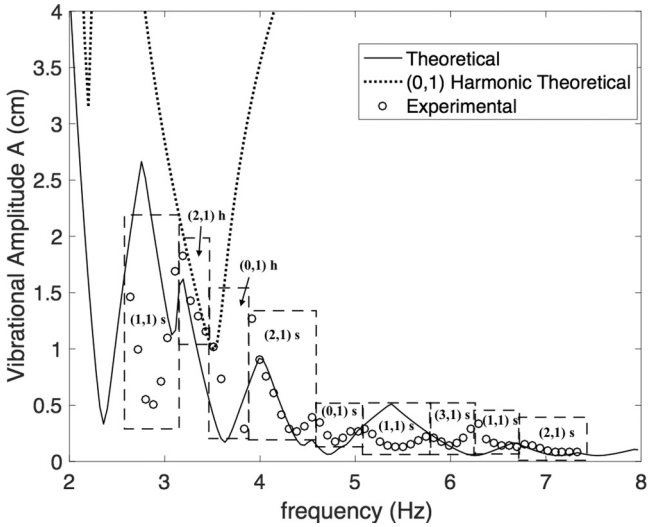

FIG. 15. Experimental results for the stability threshold obtained for the three-fluid system described in Table II in a 5.08-cm-diam cylindrical geometry. Modes are boxed by wave number, which can be compared to the theoretical predictions shown in Fig. 14. The theoretical $(0, 1)_h$ mode is also shown to account for its experimental appearance. Modal transitions and qualitative behavior are accurately predicted by the model, though quantitative agreement suffers due to the nonideal sidewall conditions.

(3.5–3.8)-Hz frequency range. Previous experiments have shown axisymmetric meniscus waves to play a destabilizing role on the $(0, 1)_h$ experimental threshold due to their shape and response harmonicity [13]. This occurs to an even greater extent in the present experiment, as both menisci are much larger than that observed in Ref. [13]. The theoretical $(0, 1)_h$ tongue is also shown on the graph for reference, and its proximity to the experimentally observed data leads to the conclusion that the destabilization is leading to its experimental presence.

In addition to the modal transitions, the experimental thresholds tend to decrease with increasing frequency, much like the theoretical predictions. Subcritical bifurcations were observed for all sections of the experimental curve with negative slopes and supercritical bifurcations were observed in positive slope sections. This observation is in agreement with previous two-fluid experiments. Codimension points were difficult to precisely excite due to the discrepancy between the theory and the experiment. In addition, out-of-phase interfacial responses were never observed experimentally. This can be attributed to the fact that the theoretically predicted out-of-phase responses typically occur at extreme values of the relative deflection, i.e., $|\phi| \ll 1$ or $|\phi| \gg 1$. In these cases, the experimentally observed modes seem to only occur on one interface, as the small deflection of the opposing interface is lost within the meniscus waves. Figure 16 shows three examples of Faraday modes obtained with the present system, each highlighting a different relative deflection type (see the Supplemental Material in Ref. [26]).

In order to minimize the adverse sidewall effects, testing was further conducted utilizing the 12.7-cm-diam cylinder. Figure 17 shows the results of this testing. As can be seen in the figure, there are multiple frequency bands where the experimental data agree with the theoretical predictions. In other zones, however, a large departure between theory and experiment is still present. The zones of agreement are those where the top interface has the dominant deflection, while the zones of disagreement are those where the bottom interface has the dominant deflection. This is indicative that the silicone oil–water interface obeys the stress-free sidewall assumption, while the water–FC-70 interface does not. In order to test this, experiments were conducted using both two-fluid pairs and compared to two-fluid theory. The results of these tests are shown in Fig. 18. These results also

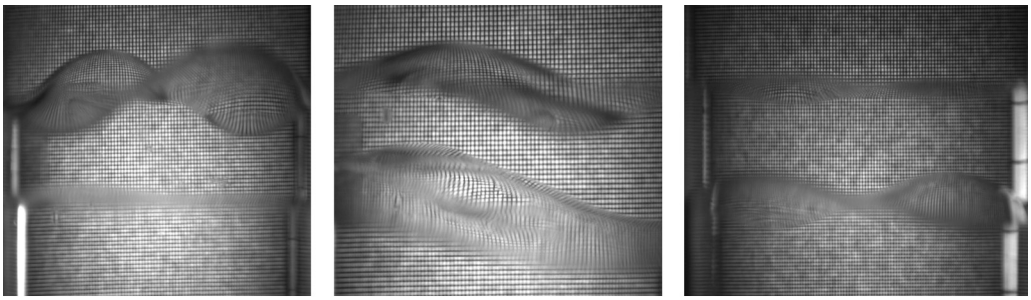

(a) (b) (c)

FIG. 16. Mode examples with large, moderate, and small relative interfacial deflection ratios. (a) The (2,1) mode with $\phi \gg 1$. The deflection of the bottom interface is much smaller than that of the top interface. The testing frequency and amplitude are 4.07 Hz and 8.6 mm, respectively. (b) The (1,1) mode with $\phi \approx 1$. Both interfaces have comparable in-phase deflections. The testing frequency and amplitude are 5.18 Hz and 4 mm, respectively. (c) The (2,1) mode with $\phi \ll 1$. The deflection of the bottom interface is much higher than that of the top interface. The testing frequency and amplitude are 6.93 Hz and 3 mm, respectively.

show excellent agreement between theory and experiment for the top two-fluid pair [Fig. 18(a)] and departure between theory and experiment for the bottom two-fluid pair [Fig. 18(b)]. For all of the 12.7-cm-diam cylinder experiments, the modal structures could not be identified due to the size of the container and competition between modes with similar wave numbers. Thus, the mode labels shown in Figs. 17 and 18 are the theoretical predictions.

Overall, the theoretical model was able to qualitatively predict the behavior of a three-fluid system with nonideal sidewall behavior. Modal transitions, with the exception of the $(0, 1)_h$ mode, were correctly predicted along with the frequency dependence of the threshold amplitude. The frequency bands where a given mode occurred were shifted to higher frequency due to the sidewall behavior, a behavior that is also seen in two-fluid systems [see Fig. 18(b)]. When utilizing the same system in a larger geometry, the agreement improved, especially for portions of the stability curve where the top interface primarily governed the stability. Full quantitative agreement between the

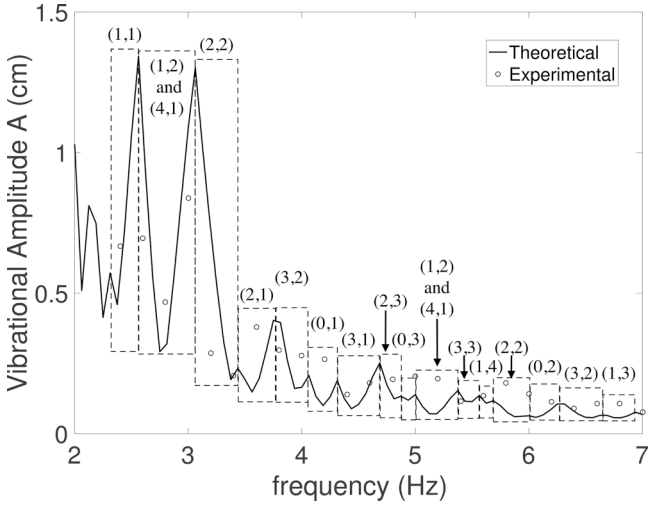

FIG. 17. Experimental results for the stability threshold obtained for the three-fluid system described in Table II in a 12.7-cm-diam cylindrical geometry. Agreement between theory and experiment is obtained in some frequency bands whose stability thresholds are primarily governed by the top interface.

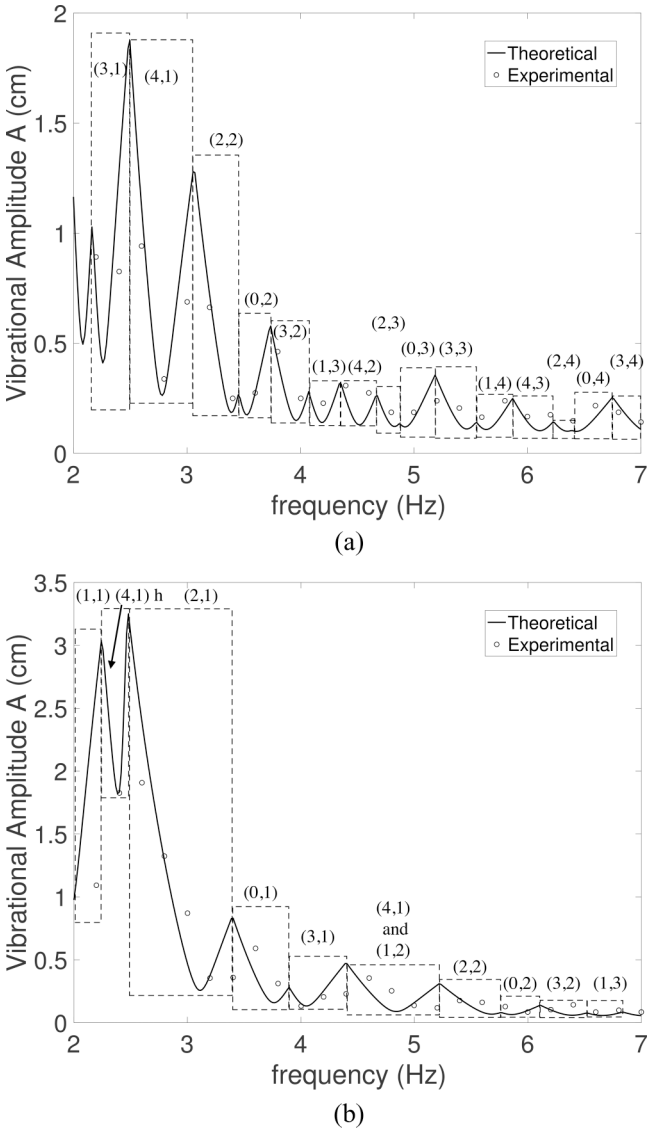

FIG. 18. Corresponding two-fluid comparisons for the system shown in Fig. 17. (a) Two-fluid comparison for silicone oil (1.905 cm) and water (1.27 cm). (b) Two-fluid comparison for water (1.27 cm) and FC-70 (1.905 cm). All of the labeled theoretical modes are subharmonic with the exception of the $(4,1)_h$ mode in (b). Agreement between theory and experiment is obtained for both systems, but to a greater extent in (a), where the stress-free sidewall assumption is better upheld.

current model and experimental data will require an ideal fluid system which upholds the stress-free sidewall condition on both interfaces or modifications to the model to account for this additional stress.

VI. CONCLUSION

In this work, the Faraday instability was studied theoretically and experimentally for mechanically oscillating three-fluid systems. The main motivation behind the work was to determine the

influence of one interface on the other, with particular interest in the enhancement or delaying of the instability solely through the addition of a third fluid. It was found theoretically that the three-fluid system produces stability tongues with multiple minima due to the multiple eigenvalue branches influenced by each interface. In extreme cases, the stability tongues can present with a single minimum similar to that seen in two-fluid problems. The behavior of the tongues with frequency and viscosity agrees with that seen in two-fluid cases. However, a disproportionate effect on one eigenvalue branch versus the other can be observed, leading to interesting behavior for some fluid combinations. Multiple codimension points unaccessible in two-fluid systems can be observed upon the addition of a third fluid. A two-fluid system can easily be destabilized through the addition of a third fluid and local stabilization can be achieved to a lesser extent by adjusting the fluid choices and layer heights. This realization could prove to be useful in processes where induced vibrations are common and the Faraday instability is undesirable, or in situations where the instability could be used to enhance a process.

Experiments were conducted in constrained geometries in an attempt to validate the model. The geometry and testing frequencies were chosen to be in the range where mode discretization was observable. Qualitative agreement was achieved, as the modal transitions, harmonicities, and threshold behavior with increasing frequency were accurately predicted. Quantitative agreement like that observed by Batson *et al.* [13] was not achievable due to the nonideal sidewall behavior caused through the addition of a third fluid. Future experiments might seek a different fluid combination to obtain better agreement between the theoretical predictions and experimentally determined thresholds. In particular, the stress-free sidewall assumption must be well realized by both interfaces in order to obtain precise agreement. Utilizing a larger geometry, where sidewall behavior became less important, improved the agreement between theory and experiment, though quantitative agreement throughout the entire stability curve was not achieved. Nevertheless, the results presented in this work should qualitatively carry over to other systems. The work presented would therefore be of practical interest for multiple applications, such as enhancing mixing in multilayer systems or the intentional suppression of the instability under conditions where its presence would be detrimental to a process through the addition of a third fluid.

This work has shown that the theory first presented by Kumar and Tuckerman [8] can effectively be extended to three-fluid cases. This results in a coupling between the fluid interfaces which must be addressed during calculation, but presents little difficulty. A good estimate for the three-fluid stability curve, however, can be obtained by superimposing two separate two-fluid calculations for the top and middle fluid and middle and bottom fluid pairs and taking the lowest of the resultant thresholds. This calculation is particularly useful for systems where the middle layer is tall, resulting in a decoupling of the interfaces.

ACKNOWLEDGMENTS

Support is acknowledged from the National Science Foundation via a Graduate Research Fellowship under Grant No. DGE-1315138, CASIS Agreement No. NNH11CD70A, NASA Grant No. NNX17AL27G, and a Chateaubriand Fellowship. F.Z. acknowledges support from CNES.

[1] M. Faraday, On a peculiar class of acoustical figures; and on certain forms assumed by groups of particles upon vibrating elastic surfaces, Philos. Trans. **121**, 299 (1831).

[2] J. W. S. Rayleigh, On the crispations of fluid resting upon a vibrating support, Philos. Mag. **16**, 50 (1883).

[3] W. S. Edwards and S. Fauve, Patterns and quasi-patterns in the Faraday experiment, J. Fluid Mech. **278**, 123 (1994).

[4] A. B. Ezerskii, P. I. Korotin, and M. I. Rabinovich, Random self-modulation of two-dimensional structures on a liquid surface during parametric excitation, Sov. Phys. JETP **41**, 157 (1985).

[5] A. Kudrolli and J. P. Gollub, Patterns and spatiotemporal chaos in parametrically forced surface waves: A systematic survey at large aspect ratio, Physica D **97**, 133 (1996).
[6] H. W. Müller, Periodic Triangular Patterns in the Faraday Experiment, Phys. Rev. Lett. **71**, 3287 (1993).
[7] T. B. Benjamin and F. Ursell, The stability of the plane free surface of a liquid in vertical periodic motion, Proc. R. Soc. London Ser. A **225**, 505 (1954).
[8] K. Kumar and L. S. Tuckerman, Parametric instability of the interface between two fluids, J. Fluid Mech. **279**, 49 (1994).
[9] H. N. Abramson, F. T. Dodge, and D. Kana, Liquid surface oscillations in longitudinally excited rigid cylindrical containers, AIAA J. **3**, 685 (1965).
[10] S. P. Das and E. J. Hopfinger, Parametrically forced gravity waves in a circular cylinder and finite-time singularity, J. Fluid Mech. **599**, 205 (2008).
[11] A. D. D. Craik and J. G. M. Armitage, Faraday excitation, hysteresis and wave instability in a narrow rectangular wave tank, Fluid Dyn. Res. **15**, 129 (1995).
[12] J. Bechhoefer, V. Ego, S. Manneville, and B. Johnson, An experimental study of the onset of parametrically pumped surface waves in viscous fluids, J. Fluid Mech. **288**, 325 (1995).
[13] W. Batson, F. Zoueshtiagh, and R. Narayanan, The Faraday threshold in small cylinders and the sidewall non-ideality, J. Fluid Mech. **729**, 496 (2013).
[14] S. Amiroudine, F. Zoueshtiagh, and R. Narayanan, Mixing generated by Faraday instability between miscible liquids, Phys. Rev. E **85**, 016326 (2012).
[15] M. Boukra, A. Cartellier, É. Ducasse, P. Gajan, M. Lalo, T. Noel, and A. Strzelecki, Use of Faraday instabilities to enhance fuel pulverisation in air-blast atomisers, C. R. Méc. **337**, 492 (2009).
[16] G. Pucci, E. Fort, M. Ben Amar, and Y. Couder, Mutual Adaptation of a Faraday Instability Pattern with its Flexible Boundaries in Floating Fluid Drops, Phys. Rev. Lett. **106**, 024503 (2011).
[17] W. Batson, F. Zoueshtiagh, and R. Narayanan, Two-frequency excitation of single-mode Faraday waves, J. Fluid Mech. **764**, 538 (2015).
[18] R. Lifshitz and D. M. Petrich, Theoretical Model for Faraday Waves with Multiple-Frequency Forcing, Phys. Rev. Lett. **79**, 1261 (1997).
[19] C. Huepe, Y. Ding, P. Umbanhowar, and M. Silber, Forcing function control of Faraday wave instabilities in viscous shallow fluids, Phys. Rev. E **73**, 016310 (2006).
[20] J. Feng, I. Jacobi, and H. Stone, Experimental investigation of the Faraday instability on a patterned surface, Exp. Fluids **57**, 86 (2016).
[21] M. Bestehorn and A. Pototsky, Faraday instability and nonlinear pattern formation of a two-layer system: A reduced model, Phys. Rev. Fluids **1**, 063905 (2016).
[22] N. Francois, H. Xia, H. Punzmann, P. W. Fontanta, and M. Shats, Wave-based liquid-interface metamaterials, Nat. Commun. **8**, 14325 (2017).
[23] L. Domino, M. Tarpin, S. Patinet, and A. Eddi, Faraday wave lattice as an elastic metamaterial, Phys. Rev. E **93**, 050202 (2016).
[24] S. Douady, Experimental study of the Faraday instability, J. Fluid Mech. **221**, 383 (1990).
[25] J. W. Miles, Nonlinear Faraday resonance, J. Fluid Mech. **146**, 285 (1984).
[26] See Supplemental Material at http://link.aps.org/supplemental/10.1103/PhysRevFluids.4.043903 for a video of interfacial behaviors.